

The effects of misaligned adherends on static ultrasonic welding of thermoplastic composites

B. G. Brito, C.; Teuwen, J.; Dransfeld, C. A.; F. Villegas, I.

DOI

[10.1016/j.compositesa.2022.106810](https://doi.org/10.1016/j.compositesa.2022.106810)

Publication date

2022

Document Version

Final published version

Published in

Composites Part A: Applied Science and Manufacturing

Citation (APA)

B. G. Brito, C., Teuwen, J., Dransfeld, C. A., & F. Villegas, I. (2022). The effects of misaligned adherends on static ultrasonic welding of thermoplastic composites. *Composites Part A: Applied Science and Manufacturing*, 155, Article 106810. <https://doi.org/10.1016/j.compositesa.2022.106810>

Important note

To cite this publication, please use the final published version (if applicable).
Please check the document version above.

Copyright

Other than for strictly personal use, it is not permitted to download, forward or distribute the text or part of it, without the consent of the author(s) and/or copyright holder(s), unless the work is under an open content license such as Creative Commons.

Takedown policy

Please contact us and provide details if you believe this document breaches copyrights.
We will remove access to the work immediately and investigate your claim.



The effects of misaligned adherends on static ultrasonic welding of thermoplastic composites

C. B. G. Brito^{*}, J. Teuwen, C.A. Dransfeld, I. F. Villegas

Aerospace Structures and Materials Department, Faculty of Aerospace Engineering, Delft University of Technology, Kluyverweg 1, 2629 HS Delft, the Netherlands

ARTICLE INFO

Keywords:

A. Carbon Fibre
C. Analytical modelling
D. Fractography
E. Joints/joining

ABSTRACT

Ultrasonic welding is a promising joining technique for thermoplastic composite parts. On the way towards upscaling and industrialisation of this technology, it is crucial to understanding how it is affected by manufacturing tolerances. The objective of the research presented in this paper was to investigate the influence that misaligned adherends have on static ultrasonic welding of thermoplastic composites. Different angles were created by changing the clamping configuration. The results showed that increasing the angle between adherends decreases the power consumed and increases the process time while decreasing the weld uniformity and increasing the risk of overheating. These effects were associated to the impact of the different clamping configurations on the cyclic strain in the energy director and adherends during the welding process. Decreasing the top adherends bending stiffness by increasing the clamping distance was found to significantly reduce the adverse effects of adherend misalignment on weld quality.

1. Introduction

The interest of the aerospace industry in thermoplastic composites has increased significantly in the last decades [1,2]. This is mostly due to the potential of thermoplastic composites to reduce manufacturing costs owing to fast manufacturing processes [3], such as press forming, and to their recyclability [4]. They also provide the possibility of using welding instead of mechanical fastening or adhesive bonding as an approach for structural joining.

Ultrasonic welding stands out from other welding methods applicable to thermoplastic composites due to its very short processing times, its capability for in-situ process monitoring and the fact that it does not need foreign materials at the welding interface [5]. Low-amplitude high-frequency mechanical vibrations are used as heat source in ultrasonic welding. To concentrate the heat generation at the welding interface, a resin-rich layer, called energy director (ED), is used between the parts to be welded. Friction and viscoelastic heating are responsible for heating up and melting the polymer of the ED and the adherends. The welded joint is established via local molecular inter-diffusion of the polymer chains in the adherends through the welding interface [6].

Several studies have been devoted to understanding the heating mechanisms that occur during ultrasonic welding [6,7,8,9,10] while others worked on improving the robustness of the process. For instance,

Villegas [11] identifies and describes five different stages that occur during the vibration phase of the process. Another work from Villegas [12] makes a direct connection between those five stages and the resulting strength of the weld. Meanwhile, others [13,14,15] investigated the influence of the energy director morphology on the process and quality of the final welds. Towards upscaling, Zhao et al. [16] studied a process control strategy for multi-spot welded joints. All this knowledge combined is of utmost importance to allow the transition from a static to a continuous process [17], since longer seams are preferred in most structural applications [18,19]. In the continuous ultrasonic welding, longer overlaps can be welded continuously because the sonotrode moves over the overlap while applying the ultrasonic vibrations and the welding force.

Up to this moment, limited attention has been given to the potential influence of manufacturing tolerances, such as a misalignment between adherends, on ultrasonic welding. In the static process, the need for parallelism between adherends is usually mentioned [20,21,22] and sometimes achieved through the use of special jigs. Still, no further investigation has been found in literature until this point. On the work of Zhao et al. [16], where sequential spot welds are studied, it is mentioned that a misalignment between the adherends is temporarily introduced for one of the jigs used on their study. They explain that the misalignment is caused by the use of a base under the top adherend that is thinner

^{*} Corresponding author.

E-mail address: c.brito@tudelft.nl (C. B. G. Brito).

<https://doi.org/10.1016/j.compositesa.2022.106810>

Received 11 June 2021; Received in revised form 12 November 2021; Accepted 8 January 2022

Available online 22 January 2022

1359-835X/© 2022 The Authors. Published by Elsevier Ltd. This is an open access article under the CC BY license (<http://creativecommons.org/licenses/by/4.0/>).

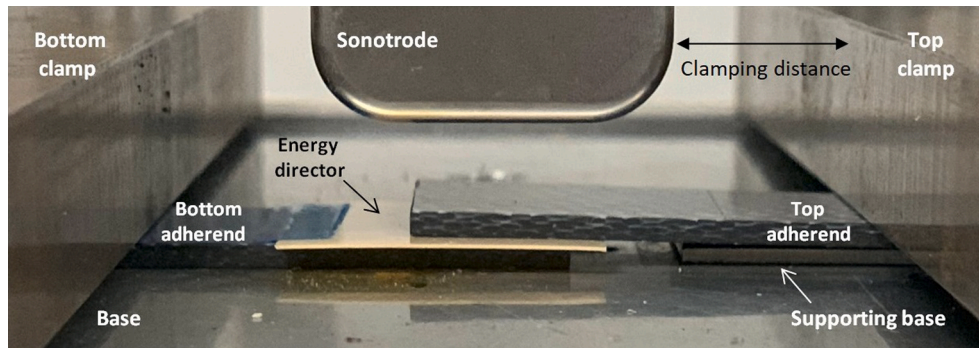


Fig. 1. Set-up of the static ultrasonic welding process. Five different supporting base thicknesses (2.15 mm, 1.90 mm, 1.50 mm, 1.25 mm and 0.00 mm) and two clamping distances (5 mm and 50 mm) were used.

Table 1

Summary of welded joints obtained in this study.

Clamping case	Welding force (N)	Welding amplitude (μm)	Displacement	Consolidation phase	Number of welded joints	Analysis
1.00/5	500	86.2	OoF ¹	Yes	3	Power/displacement
0.88/5			Full ²	Yes	3	Power/displacement and temperature
			OoF ¹	No	1	Fractography
			Full ²	Yes	3	Power/displacement and temperature
0.70/5	500	86.2	OoF ¹	No	1	Fractography
			Full ²	Yes	3	Power/displacement and temperature
			OoF ¹	No	1	Fractography
			OoF ¹	Yes	1	Cross-section microscopy
1.00/50	500	86.2	OoF ¹	Yes	3	Power/displacement
0.88/50			Full ²	Yes	3	Power/displacement and temperature
			OoF ¹	No	1	Fractography
			OoF ¹	Yes	1	Cross-section microscopy
	500	86.2	d _{opt} ³	Yes	3	Weld strength and fractography
			Full ²	Yes	3	Power/displacement and temperature
			OoF ¹	No	1	Fractography
			d _{opt} ³	Yes	3	Weld strength and fractography
0.70/50	500	86.2	Full ²	Yes	3	Power/displacement and temperature
			OoF ¹	No	1	Fractography
			d _{opt} ³	Yes	3	Weld strength and fractography
			Full ²	Yes	3	Power/displacement and temperature
0.00/50	500	86.2	OoF ¹	No	1	Fractography
			d _{opt} ³	Yes	3	Weld strength and fractography

¹ OoF stands for Onset of Flow, defined in this work as downward sonotrode displacement = 0.03 mm.

² Full corresponds to downward sonotrode displacement that equals the thickness of the ED (0.25 mm).

³ d_{opt} stands for optimum sonotrode displacement (see Section 2.2).

than the bottom adherend. Although the authors claim that the misalignment was corrected once the sonotrode applied the welding force on the overlap, this statement was not checked or further investigated. Nevertheless, they show that a misalignment later introduced by the welding of sequential spots can be expected to have an impact on the welded area. According to Eveno and Gillespie [23], areas with higher pressure will focus cyclic stress, melting faster than the rest of the overlap, since the viscoelastic heating rate is dependent on the cyclic strain in the energy director. It is therefore reasonable to expect that a misalignment between top and bottom adherends will result in heterogeneous melting of the overlap area, potentially having an impact in the final quality of the joint. The use of misaligned adherends might also affect other parameters of the ultrasonic welding process, such as the amplitude of vibration. Villegas [11] showed that the amplitude of vibration affects the duration and magnitude of the power consumed during the five stages of the process when either high and low welding force were used. Since the amplitude of vibration affects the stress experienced by the parts [24], it is natural to expect that an uneven application of the amplitude of vibration will have some impact on the process. Understanding the implications caused by misaligned adherends is necessary for the industrialisation of ultrasonic welding, since the process will most likely be employed on curved parts, such as an aircraft fuselage, where clamping conditions are limited and where the sonotrode is moveable and hence more susceptible to tilting and asymmetries in its positioning [25,26].

To increase the existing knowledge on the effect of manufacturing tolerances on ultrasonic welding of thermoplastic composites, our objective in this work is to investigate the influence of the presence of an angle between adherends on the welding process. To obtain different angles between adherends, we worked with different clamping configurations. Side-view pictures of the overlap were used to quantify the misalignment between the adherends and the area of the top adherend that was in contact with the sonotrode was measured. To assess how the welding process was affected by the angle between adherends, the consumed power and the vertical displacement of the sonotrode during welding were analysed. Fracture surface and cross-sectional analysis, temperature measurements at the welding interface and a finite element model were used for further insight.

2. Methodology

2.1. Materials and manufacturing

The specimens were manufactured using Toray Cetex® TC1200 carbon 5-harness satin fabric reinforced polyetheretherketone (C/PEEK) from Toray Advanced Composites (the Netherlands). The carbon fibre was T300JB with a nominal fibre volume content of 50%. The laminates, with a [(0/90)₃]_s stacking sequence and 1.9 mm nominal thickness, were consolidated in a hot platen press at 385 °C and 10 bar for 30 min. From the consolidated laminate, adherends of dimensions 25.4 mm by

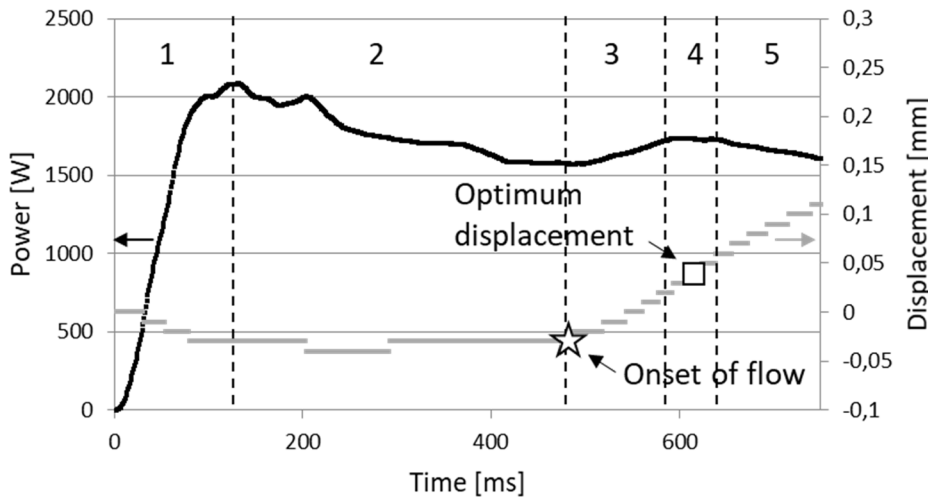


Fig. 2. Typical power and displacement curves for C/PEEK laminates (86.2 μm vibration amplitude, 500 N welding force, 0.25 mm sonotrode displacement, 0.88 normalised base thickness, 50 mm clamping distance). Note: downward displacement of sonotrode is represented as positive displacement in this graph. Five stages are identified: 1) Initial heating of the ED; 2) Gradual melting of the ED; 3) Onset of the squeeze flow of the molten ED; 4) Melting of the first layers of the adherends (optimum weld quality); and 5) bulk heating in the adherends [11].

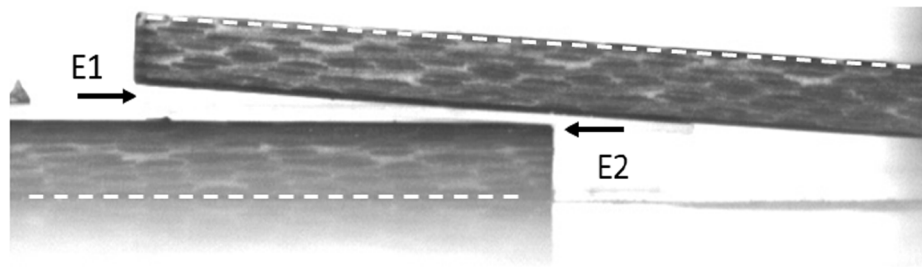


Fig. 3. Side view of overlap where the white dashed lines indicate the two arms that compose the angle to be measured. E1 and E2 indicate the transverse edges of the overlap.

101.6 mm were cut with a water-cooled diamond blade. The adherends were cut with their longitudinal edge along the warp direction of the weave. For the ED, a 0.25 mm-thick flat film of neat PEEK resin supplied by Goodfellow Cambridge Ltd (England) was used.

2.2. Ultrasonic welding process

The adherends were welded into a single-lap configuration (overlap of 12.7 mm length and 25.4 mm width) with a 20 kHz ultrasonic welding machine (HiQ DIALOG SpeedControl Herrmann Ultraschall, Germany) and a rectangular sonotrode with a 15 mm by 30 mm contact area. Based on previous research on ultrasonic welding of thermoplastic composites [13,14,15], the peak-to-peak amplitude of vibration was set to 86.2 μm and the welding force was 500 N in all cases. Note that as shown in [11,12] a wide range of amplitude and force combinations allow obtaining similar high-strength welded joints. The duration of the vibration phase of the welding process was indirectly controlled through the vertical displacement of the sonotrode. In some cases, the vibration phase was followed by a consolidation phase in which the welded joint was allowed to cool down subjected to 500 N for 4 s. In other cases, the process was stopped right after the end of the vibration phase in order to prevent any further squeeze flow during consolidation and hence to preserve the “squeeze flow scenario” resulting from the vibration phase. Fig. 1 shows the jig used to hold the adherends during the static ultrasonic welding process, composed of two bar clamps. The distance of the bar clamping the top adherend (top clamp) to the sonotrode, called *clamping distance* hereafter, was either 5 mm or 50 mm. The distance from the bar clamping the bottom adherend (bottom clamp) to the sonotrode remained at 25 mm for all tests. Five different thicknesses were used for the supporting base underneath the top adherend (see Fig. 1): 2.15 mm, 1.90 mm, 1.50 mm, 1.25 mm and 0.00 mm. Normalised base thickness values were calculated by dividing the thickness

of the supporting base by the thickness of the bottom adherend plus the thickness of the ED (2.15 mm in total). The normalised base thickness values were: 1.00, 0.88, 0.70, 0.58 and 0.00. It should be noted that a normalised base thickness of 1.00 will not induce any angle between the top and bottom adherends, whereas a normalised base thickness below 1.00 will induce an angle between the adherends which will increase as the thickness of the supporting base decreases. The nomenclature *Normalised thickness of the supporting base* (unitless)/*Clamping distance* (mm) is used hereafter when mentioning the different clamping cases used in this study (see Table 1).

The power and vertical displacement of the sonotrode during the vibration phase of the welding process were given by the welding machine as outputs and are referred to as *power and displacement curves* (Fig. 2). Five stages can be identified, corresponding to the physical changes occurring in the ED and adherends as a result of the ultrasonic vibration [11,12]. Of particular importance for this research are the *onset of the flow* and the *optimum displacement* (Fig. 2). The onset of the flow is defined by the moment when the sonotrode starts displacing downwards (i.e. the end of stage 2), which is related to molten polymer, generally the ED, starting to be squeezed out of the welding overlap [11]. Optimum displacement is the displacement which results in welds with the highest weld strength and it is found within stage 4 of the process (see Fig. 2) [12]. Whilst the importance of the optimum displacement and maximum weld strength are obvious, monitoring the process until the onset of flow was of interest in this work since: (1) the maximum power consumed by the process (referred to as *power peak*) is usually observed before the onset of the flow, and (2) the time until the onset of the flow generally plays the biggest role in the total duration of the vibration phase. As a general procedure in this work, the onset of the flow was determined according to Fig. 2. When stopping the welding process at the onset of the flow, a downward displacement of the sonotrode of 0.03 mm was used due to practical reasons. The optimum

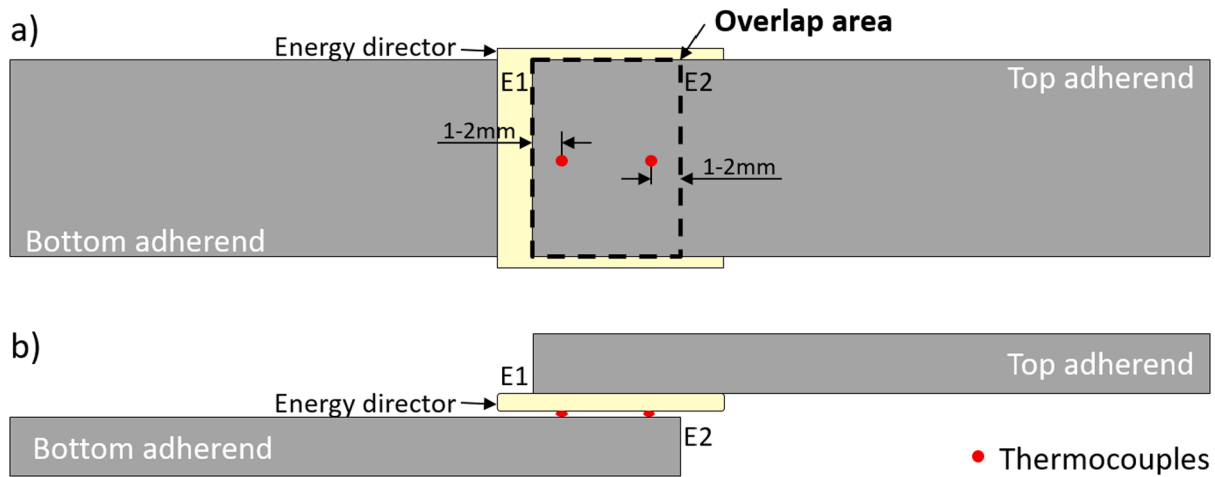


Fig. 4. a) Top-view and b) side-view schematic of the position of the thermocouples for temperature measurements. The thermocouples were placed 1–2 mm away from the transversal edges of the overlap (E1 and E2).

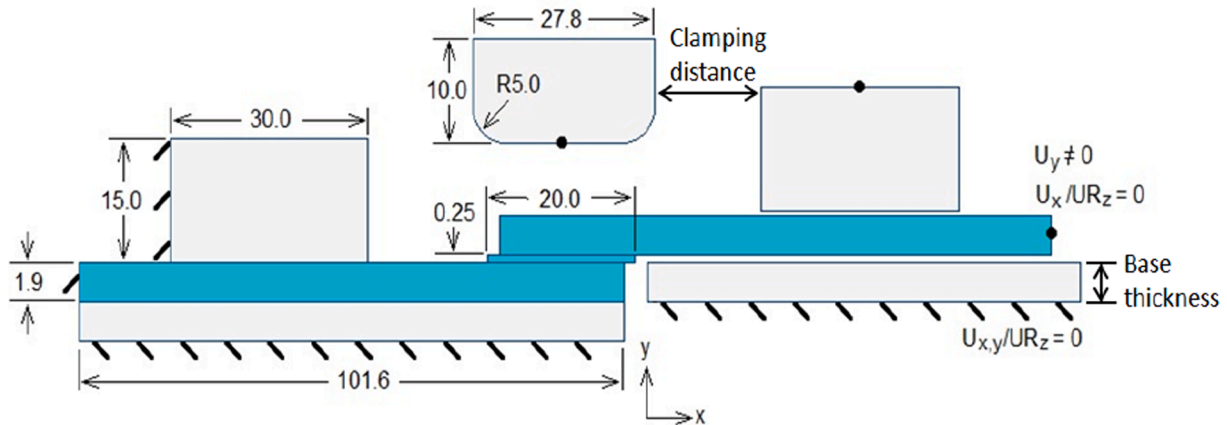


Fig. 5. 2D FEM model of the ultrasonic welding set-up with dimension of parts, boundary conditions, clamping distance (5 mm or 50 mm) and supporting base thickness (2.15 mm, 1.90 mm, 1.50 mm, 1.25 mm or 0.00 mm). Grey parts were modelled as rigid bodies while blue parts were meshed. Dimensions are in [mm].

displacement was defined following the procedure described by Villegas [12]. It should be noted that, owing to its higher practical significance, optimum displacement values were only defined in those cases in which a fully welded overlap was achieved.

2.3. Angle, contact area and temperature measurements

The angle between top and bottom adherends was measured with ImageJ (version 1.52a) on high-resolution pictures of the overlap (Optomotive high-resolution digital camera, Mechatronics Ltd). To determine the angle between adherends in each clamping case, three repeats of angle measurements were made using a different top adherend in each one of them. The angle was measured before the application of the welding force using the bottom surface of the bottom adherend and the top surface of the top adherend (Fig. 3). These outer surfaces were chosen to measure the angle since, in some occasions, the energy director (which was larger than the overlap) was found to (partially) block the view of the inner surfaces. The two transverse edges of the overlap, denoted as *Edge 1* (E1) and *Edge 2* (E2) hereafter, are also indicated in Fig. 3. Edge 1 corresponds to the location of the free end of the top adherend while Edge 2 corresponds to the free edge of the bottom adherend.

As an important element in the transmission of the ultrasonic vibration and of the welding force to the welding interface, the contact area between the sonotrode and the top adherend was measured in all

the different clamping cases in this study. For this purpose, a 0.15 mm-thick double-sided adhesive tape was bonded to the top surface of the top adherend. A black marker pen was used to paint the bottom surface of the sonotrode. After the sonotrode had come into contact with the top adherend and applied the prescribed welding force, the contact area could be visualised by the black ink transferred onto the double-sided tape upon retraction of the sonotrode. Three repeats of contact area measurements, each one with a different top adherend, were performed for each clamping case. Three different top adherends were used for each clamping case. A calliper was then used to measure the dimensions of the resulting imprint. The percentage contact area was obtained by dividing the average area of the imprints by the maximum contact area.

Finally, to assess the effect of the angle between the adherends on the temperature evolution at the longitudinal edges of the overlap, two 0.1 mm-thick K-type thermocouples were used. With the bottom adherend clamped to the base of the jig (see Fig. 1), the thermocouples were placed on its top surface. Their measuring tips were located within the overlap and 1–2 mm away from Edge 1 and Edge 2, and on the longitudinal midline of the adherend (Fig. 4). The thermocouples were secured in place by adhesive tapes placed outside the overlap. After proper positioning of the thermocouples, the energy director was placed on top of the them. Finally, the top adherend was clamped in place (see Fig. 1). The temperature was sampled at a rate of 1 kHz. Table 1 summarises the experiments in which temperature measurements were performed.

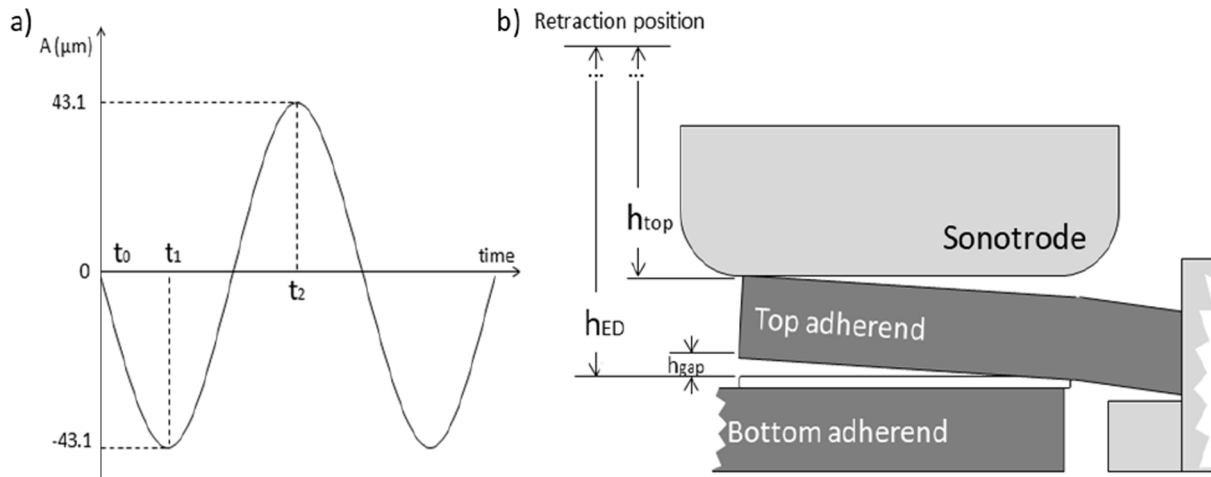


Fig. 6. Schematic representation of a) the sinusoidal movement of the sonotrode and the different positions that were simulated in Steps 2, 3 and 4 of the model and b) the different heights used to determine the h_{gap} that was used as input in Step 2 of the FEM model.

Table 2

Difference in height between ED and top adherend at Edge 1 of the overlap (h_{gap}) for the different clamping combinations used in the model.

Case	0.88/50	0.70/50	0.00/50	0.88/5	0.70/5	0.58/5
h_{gap} [mm]	0.0033	0.0050	0.0117	0.0050	0.025	0.1417

2.4. Mechanical testing, fractography and microscopy characterisation

Single-lap shear tests were performed to quantify the weld strength (in those cases in which a full welded overlap could be achieved) and to obtain access to the fracture surfaces (see Table 1) and hence to gain information about the physical changes occurring at the welding interface. A Zwick/Roell 250kN universal testing machine operated at a crosshead speed of 1.3 mm/min was used. Naked-eye fractography was performed after the mechanical tests in order to determine the uniformity and amount of welded area. The lap shear strength (LSS) of the welded joints was calculated as the maximum load registered in the test divided by the total overlap area.

Cross-section microscopy was used to analyse some of the welded joints (see Table 1). For this purpose, the as-welded samples were cut along the longitudinal midline of the overlap with a water-cooled Secotom-10 precision cutting machine in order to minimize damage on the material. They were then embedded in epoxy resin and grinded and polished with a Struers Tegramin-20 polisher. A Keyence VH-Z100UR digital microscope was used for the observation of the cross-sections. Note that any potential damaged material from the cutting process was most likely removed in its entirety through the subsequent grinding and polishing process.

2.5. Finite element model

To gain a deeper understanding of the strains imposed on the ED as a result of the ultrasonic vibration, a finite element method (FEM) model was created using Abaqus FEA 2019. The welding set-up was recreated as simplified 2D model (Fig. 5) using surface-to-surface contact formulations. The clamp position and the supporting base thickness were varied to simulate each clamping combination. In this model the sonotrode, the base of the jig, the supporting base under the top adherend and the bar clamps were simulated as rigid parts. In turn, the adherends and the ED were simulated as 2D linear deformable parts and were provided with a refined mesh. The ED was divided into 100 rectangular elements along its length and 1 across its thickness while the adherends were meshed with 26 rectangular elements within the overlap length per

3 rectangular elements across its thickness. As a simplified model, the ED and the adherends were simulated as isotropic materials with Young modulus of 3.7GPa [27] and 11GPa, respectively. Note that the Young modulus of the adherends was obtained using the rule of mixtures (with 3.7GPa [27] and 180GPa [28] as the Young's modulus of matrix and fibres, respectively). A Poisson ratio of 0.4 was used for both materials [27]. Due to the sample geometry, plane strain was assumed [28].

To translate a dynamic process into a static simulation, analyses were carried out in four load steps. Step 1 describes the clamping of the top adherend and was simulated by vertically moving the top clamp downwards. Due to the difference in height between the top surface of the bottom adherend-ED stack and the top surface of the supporting base, the top clamp deforms the top adherend until it gets in contact with the supporting base. The resulting state corresponds to the setup ready for the welding process to start. Steps 2, 3 and 4 describe the different positions of the sonotrode during the vibration phase. In step 2 the sonotrode is at its neutral position (vertical displacement $y = 0 \mu\text{m}$, t_0 in Fig. 6.a). Step 3 describes the lowest position of the sonotrode during the vibration ($y = -43.1 \mu\text{m}$, t_1 in Fig. 6.a). Step 4 describes the highest position of the sonotrode during the vibration ($y = +43.1 \mu\text{m}$, t_2 in Fig. 6.a).

To simulate Step 2, the neutral position of the sonotrode needs to be defined. This was done by calculating the height of the gap that remains between the top adherend and the energy director when the welding force is applied (h_{gap} , Fig. 5.b). This was done by first measuring the distance travelled by the sonotrode from its retracted position until it touched the energy director (h_{ED} , Fig. 6.b) when the top adherend was removed from the setup. And second, by measuring the distance travelled by the sonotrode from its retracted position until it touched the top adherend (h_{top} , Fig. 6.b). The height of the gap was then calculated $h_{\text{gap}} = h_{\text{ED}} - h_{\text{top}} - \text{average thickness top adherend}$. Only the clamping cases that induce an angle between the adherends, i.e., normalised base thickness < 1.00 , were simulated. Table 2 shows the resulting h_{gap} values for each one of these cases.

3. Results

3.1. Angle and contact area

Fig. 7 shows the angle between top and bottom adherends and the contact area between sonotrode and top adherend for the different clamping cases under consideration. It is possible to see from Fig. 7.a that the 2.15 mm-thick supporting base (normalised thickness = 1.00) is the only one that resulted in similar angles, very close to 0° , for both 5 mm and 50 mm clamping distances. For all other supporting base

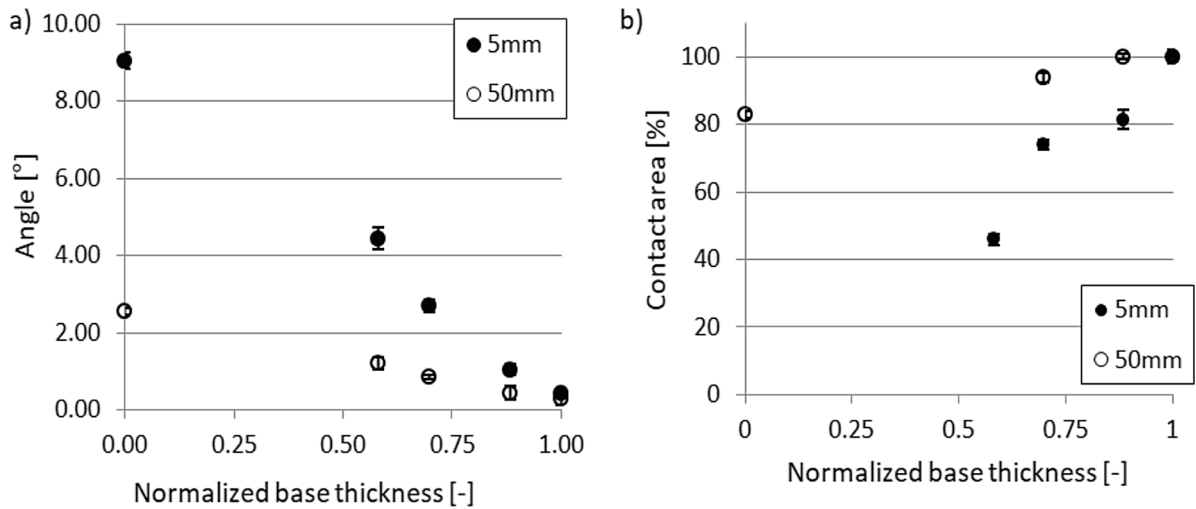


Fig. 7. a) Angle between adherends versus specific supporting base thickness for different clamping distances. b) Contact area during the application of the welding force (500 N) versus specific supporting base thickness for different clamping distances.

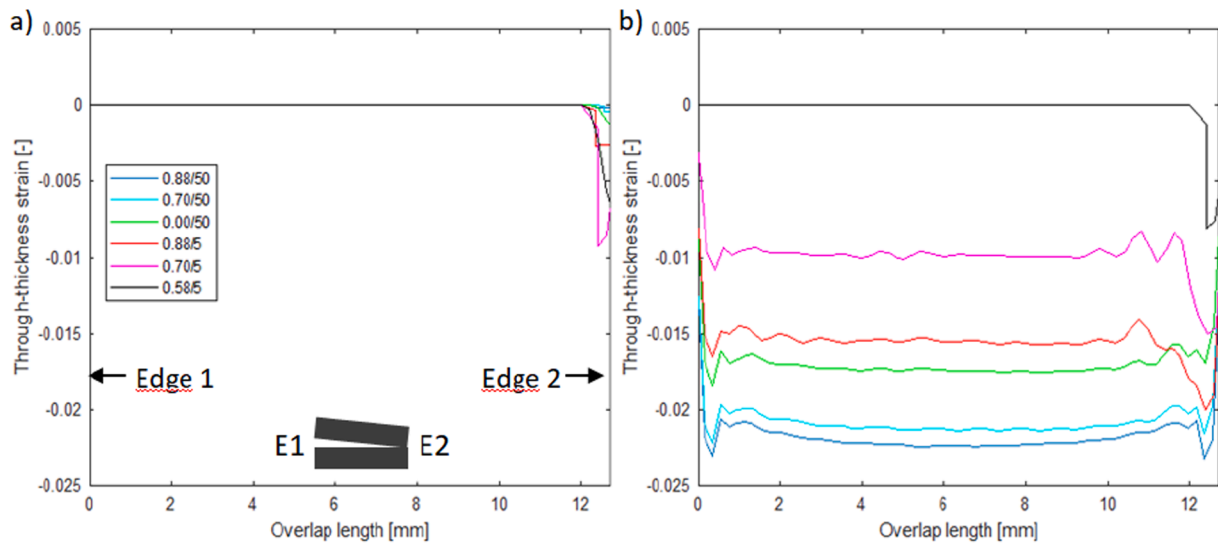


Fig. 8. Through-thickness strain at a) highest and b) lowest positions of the sonotrode for different clamping combinations. Legend and schematic of overlap apply for both graphs.

thicknesses, the angles obtained with the 5 mm clamping distance were at least 2 times larger than those obtained for 50 mm clamping distance. Regarding the contact area, Fig. 7.b shows that the 2.15 mm supporting base is the only one that resulted in contact areas of 100% for both 5 mm and 50 mm clamping distances. For all the other supporting bases, the contact areas obtained with the 5 mm clamping distance were at least 20% smaller than those for 50 mm.

3.2. Numerical through-thickness strain

Fig. 8 shows the magnitude of the through-thickness strain on the ED when the sonotrode is at its highest and lowest positions (corresponding to + 43.1 μm and -43.1 μm in the vibration cycle, respectively (see Fig. 5.a) for different clamping cases. It is possible to see that at the highest position of the sonotrode, shown in Fig. 8.a, all cases present an overall null strain in the overlap, except around Edge 2, where a localised compressive strain can be observed for the cases with the shortest clamping distance (5 mm). At the lowest position of the sonotrode, shown in Fig. 8.b, the overall compressive strain (edges of the overlap not considered) is higher for the longest clamping distance (50 mm) and

increases with increasing thickness of the supporting base. The overall strain is mostly constant but it fluctuates at the edges of the overlap for all clamping cases. A localised compressive strain at Edge 2 is again observed only for the cases with the shortest clamping distance (5 mm). The difference between the strain at the lowest and at the highest positions of the sonotrode calculated along the overlap, discarding the variations observed at the overlap edges, results in the through-thickness cyclic strain. This calculation gives the through-thickness cyclic strain along most of the length of the overlap, which is then averaged, resulting in an approximate value of through-thickness cyclic strain for each case. This averaged value will be used in the analytical model presented on Appendix A, providing an estimation of time to flow and power peak for the different cases.

3.3. Welding process

Fig. 9a and 8.b show the power curves until the onset of the flow obtained from welds with 5 mm and 50 mm clamping distance, respectively, while the supporting base thickness was varied. A general increase in the time to flow and a decrease in the magnitude of the power

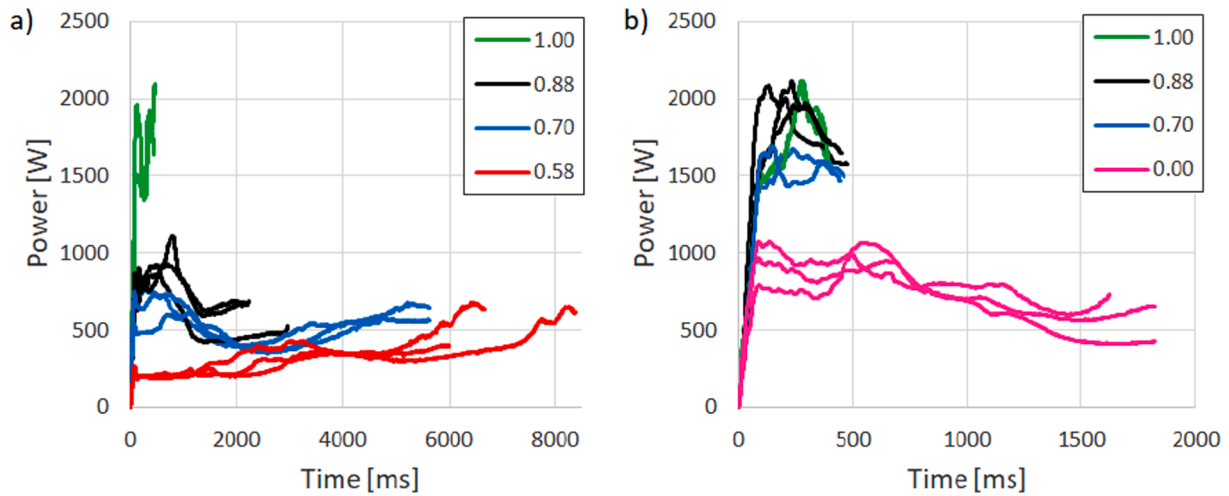


Fig. 9. Power consumed versus time for a) 5 mm and b) 50 mm clamping distance and different specific supporting bases thicknesses. The curves span from the beginning of the vibration phase until the onset of the downward displacement of the sonotrode (i.e. onset of flow).

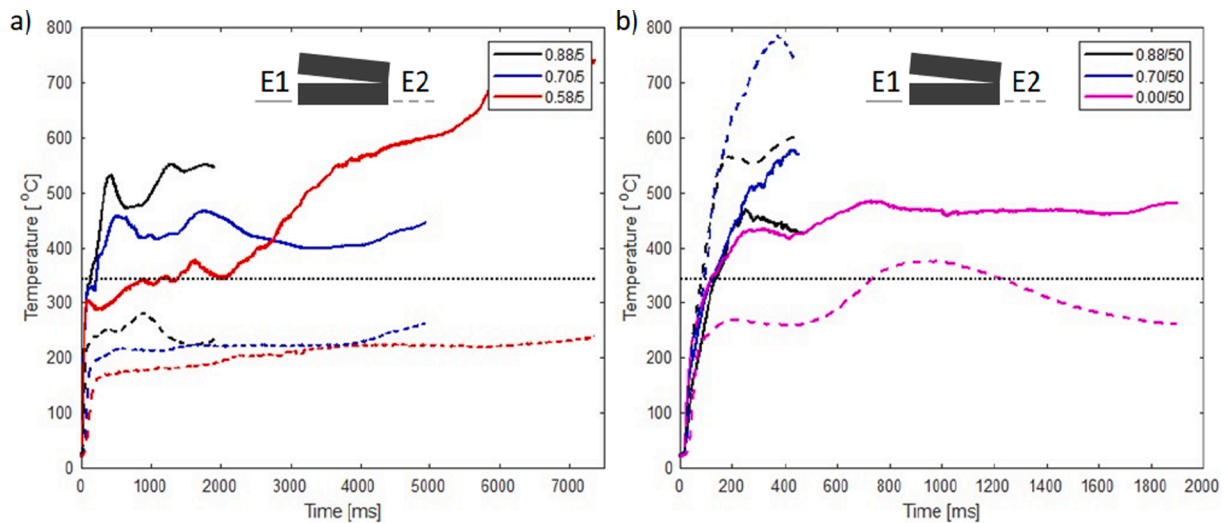


Fig. 10. Temperature records at Edges 1 (solid lines) and 2 (dashed lines) for a) 5 mm and b) 50 mm clamping distance and different supporting base thicknesses. All welds were stopped at the onset of the flow. The dotted line corresponds to the melting temperature of PEEK (343 °C).

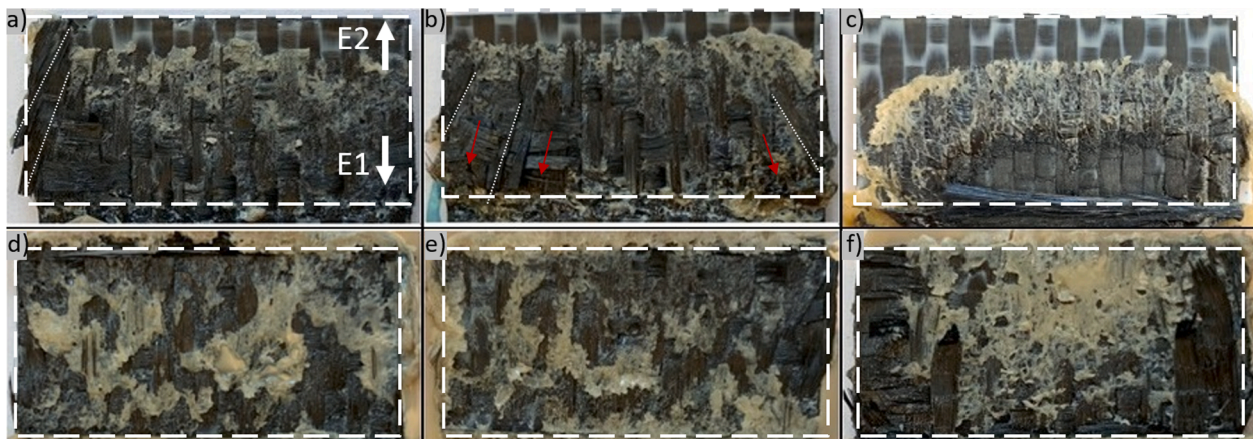


Fig. 11. Fracture surfaces of welds stopped at the onset of flow for a) 0.88/5, b) 0.70/5, c) 0.58/5, d) 0.88/50, e) 0.70/50 and f) 0.00/50 clamping cases. The fracture surfaces correspond to the bottom adherend welded area and no consolidation phase was applied. Dashed rectangles indicate the overlap area. Position of Edge 1 and Edge 2 for all fracture surfaces is indicated in a). The dotted lines indicate the misaligned fibre bundles and the red arrows indicate discoloration of the resin.

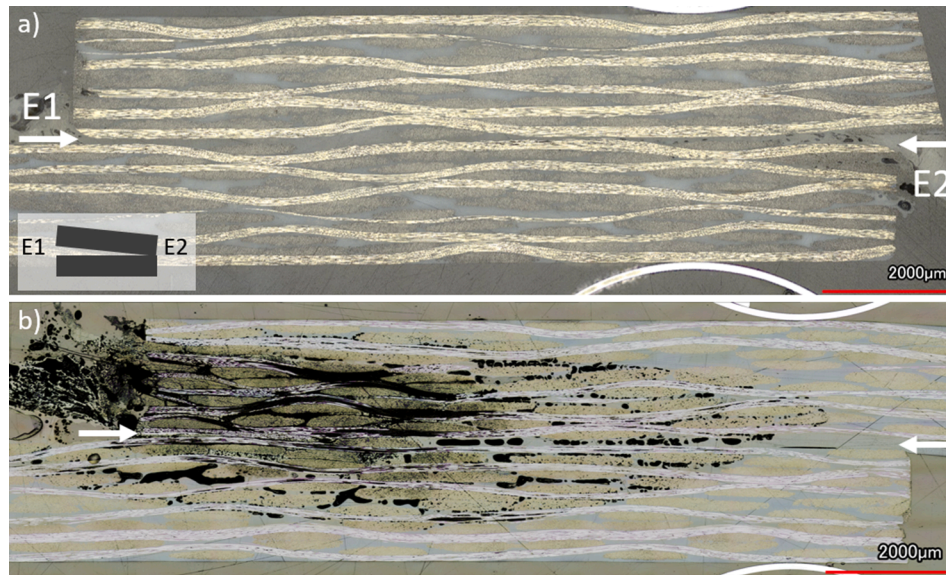


Fig. 12. Cross-sectional micrograph (side-view) of a process stopped at the onset of flow for a) 0.88/50 and b) 0.58/5. Consolidation phase was applied. The arrows indicate the location of the weld line.

peak when decreasing the thickness of the supporting base is observed. These two effects are more pronounced for the shortest clamping distance. The values of time to flow and power peak obtained from these curves are shown in Table 3.

3.4. Temperature measurements

The temperature evolution at Edges 1 and 2 of the overlap until the onset of the flow is shown in Fig. 10 for the different clamping cases. At the shortest clamping distance (Fig. 10.a), the temperature at Edge 2 is consistently lower than the temperature at Edge 1 for all three base thicknesses considered. The temperatures at both edges are higher for increasing base thickness and in none of the cases reach the melting temperature of PEEK ($T_m = 343^\circ\text{C}$) at Edge 2. At the longest clamping distance (Fig. 10.b) the temperature at Edge 2 is only lower than the temperature at Edge 1 in the case in which no supporting base was used (base thickness equals zero). For the other two base thicknesses, the opposite trend is observed. Moreover, the temperature in both edges for the different base thicknesses exceeds the PEEK T_m eventually.

3.5. Fracture surfaces and cross-section microscopy

Fracture surfaces of samples welded up to the onset of flow at the shortest clamping distance (Fig. 11.a, 11.b and 11.c) feature a non-uniform appearance, which is more pronounced as the thickness of the base decreases. It should be noted that none of the samples shown in Fig. 11 underwent consolidation after the vibration phase (see Table 1), hence the unusual appearance of the fracture surfaces as compared to those corresponding to consolidated welds [12]. Three distinct areas can be identified on these fracture surfaces. The first area, corresponding to Edge 2 of the overlap, is characterised by intact adherend. The second area, found as one moves towards the opposite edge of the overlap, Edge 1, presents a mix of exposed fibres and resin-rich failure. Finally, the third area, located at Edge 1, especially evident in the two lowest base thicknesses (Fig. 11.b and 11.c), is characterised by exposed fibres. Discoloration is observed in the resin squeezed out of the overlap at Edge 1, as indicated by the red arrows in Fig. 11.b. Misaligned fibre bundles are also present for some cases and are indicated in Fig. 11 by the dotted lines. Contrarily, fracture surfaces of samples welded at the longest clamping distance (Fig. 11.d, 11.e and 11.f) feature a fairly uniform appearance with a mix of resin-rich failure and exposed fibres in the

entire overlap area.

Cross-sectional micrographs in the longitudinal direction of the overlap of welded joints corresponding to the smallest and the biggest angles in this study (0.88/50 and 0.58/5, see Fig. 7) are shown in Fig. 12. The reader should note that in those cases, unlike in the cases shown in Fig. 11, consolidation was applied after the vibration phase ended (right after the onset of the flow) to discard deconsolidation as the source of porosity. It should also be noted that the application of the consolidation force resulted in extra squeeze flow as compared to those cases with no consolidation phase (Fig. 11). The main characteristic of the cross-section corresponding to the smallest angle (0.88/50 case, Fig. 12.a) is the complete absence of porosity in both the adherends and in the weld line. On the other hand, the cross-sectional micrograph corresponding to the biggest angle (0.58/5 case, Fig. 12.b) features three distinct areas, which is consistent with the features on the fracture surface in Fig. 11.c (same clamping conditions). The first area in Fig. 12.b, corresponding to Edge 2 of the overlap, shows intact adherends and energy director. Moving towards Edge 1, the second area presents an increased number of voids at the welding interface and at the inner layers of both adherends. At the third area, located at Edge 1, extreme porosity is observed through the entire thickness of the top adherend, with squeeze flow of the matrix from the top adherend and, presumably the ED, resulting in resin flash at its free edge.

3.6. Optimum welds

The cases with the longest clamping distance (50 mm) were the ones that had the highest potential to achieve high-strength welded joints, since they featured fully welded overlaps and the most uniform fracture surfaces in Fig. 11 (Fig. 11.d, 11.e and 11.f). Consequently, samples were welded in optimum conditions (i.e., optimum vibration or heating time indirectly controlled by downward displacement of sonotrode) for these three cases and they were subsequently mechanically tested in order to evaluate how the angle affects the optimum heating time and weld strength. The results of those tests are shown in Table 4 with representative fracture surfaces, the angle between the adherends, optimum displacement of the sonotrode and heating time (i.e. duration of the vibration phase as output provided by the welder). The fracture surfaces of these optimum welds show that, as expected from results in Fig. 11, the entire overlap area was welded and they look fairly uniform. The fracture surface of case 0.00/50 is the only one that slightly differs from

Table 3

Power peak and time to flow for the different cases studied in this work.

Case	Power peak* [W]	Time to flow [ms]
1.00/50	2095.50 ± 23.30	406.00 ± 36.80
0.88/50	2052.00 ± 80.13	444.00 ± 41.94
0.70/50	1681.00 ± 5.66	449.50 ± 6.72
0.00/50	1002.67 ± 60.67	1963.00 ± 429.96
1.00/5	1892.50 ± 91.20	420.00 ± 24.00
0.88/5	989.00 ± 106.66	2442.00 ± 468.85
0.70/5	706.67 ± 85.05	4937.00 ± 598.68
0.58/5**	384.67 ± 39.46	7367.67 ± 900.59

* The power peak was defined as the maximum value of power until the onset of the flow.

** Case 0.58/5 replaces case 0.00/5 because the time to flow of the latter exceeded the time limit of the welding machine, i.e. 16000 ms.

the other two, with failure occurring at deeper layers within the adherend towards Edge 1.

4. Discussion

The objective of this paper is to understand how the presence of an angle between the adherends affects the static ultrasonic welding process. In particular the effects of the angle between adherends on the time to flow, the maximum consumed power and the weld uniformity were assessed. Different angles, which were quantified by the use of side-view pictures, were obtained by varying the clamping distance and the thickness of the supporting base. The changes in the time to flow and in

the maximum consumed power were assessed using the output data for the ultrasonic welder. Weld uniformity was assessed using fractography and cross-section microscopy. Numerical calculations of the compressive strain in the ED, temperature measurements at the welding interface and the measured contact area between top adherend and sonotrode were also used to understand those effects.

To assess the relationship between *time to flow* and *power peak* and the angle of the adherends, the information in Fig. 7.a and Table 3 are combined in Fig. 13. As seen in this Figure, general trends where time to flow increases and power peak decreases with increasing angle are observed. However, because a linear relationship is not obtained, it is hypothesised that the clamping distance has an additional effect on such relationships other than just causing a change in the angle between the adherends. Such additional effect could be related to the change in the vibration properties, i.e. damping coefficient and spring constant, of the top adherend when varying the clamping distance. If that were the case, a change in the clamping distance should result in changes in the time to flow and power peak even for the cases where the adherends remain parallel to each other for both clamping distances (i.e., normalised supporting base thickness equal to 1.00). That is not the case, since, as seen in Fig. 13, the 1.00/5 and 1.00/50 cases show no considerable differences on time to flow and power peak despite the significant change in clamping distance. Thus, the hypothesis regarding the clamping distance affecting the vibration properties of the top adherend is invalidated. Another possible explanation is that the angle between adherends by itself is not indicative of the effect of the clamping distance on the deflection of the top adherend under the welding force and,

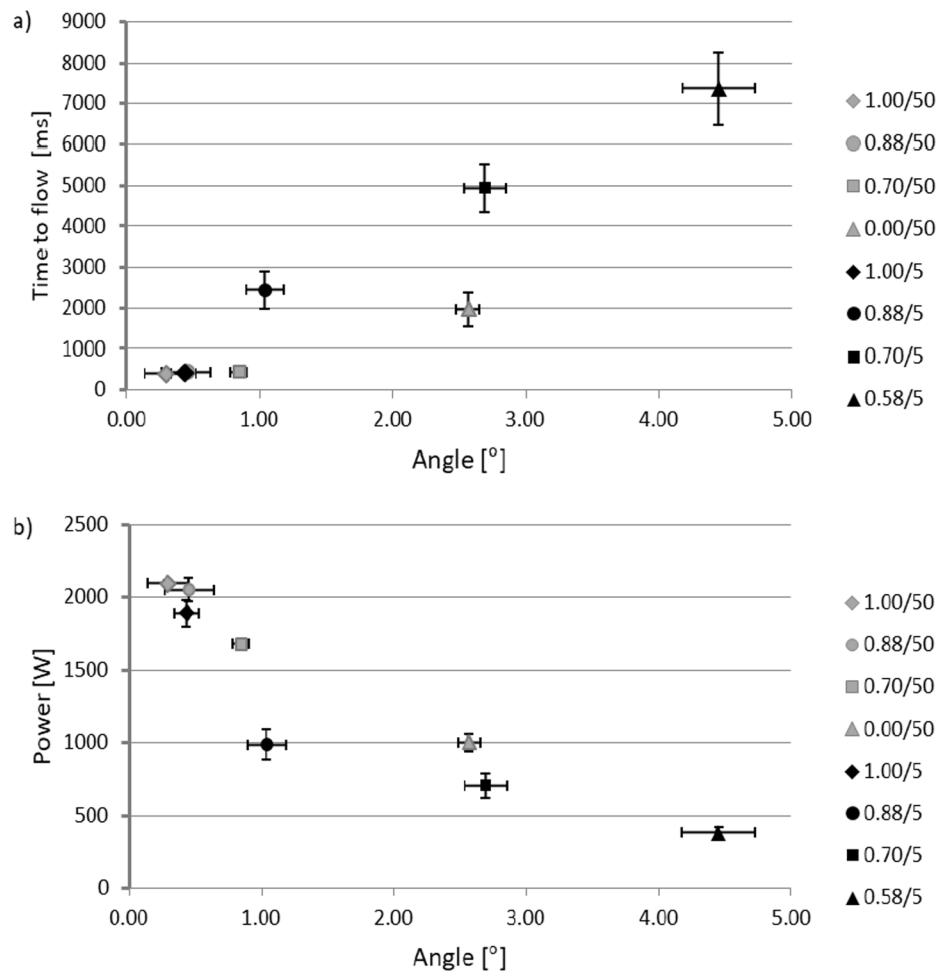


Fig. 13. a) Time to flow and b) Power peak versus angle for different clamping combinations. Welding parameters are 500 N welding force and 86.2 μm amplitude of vibration.

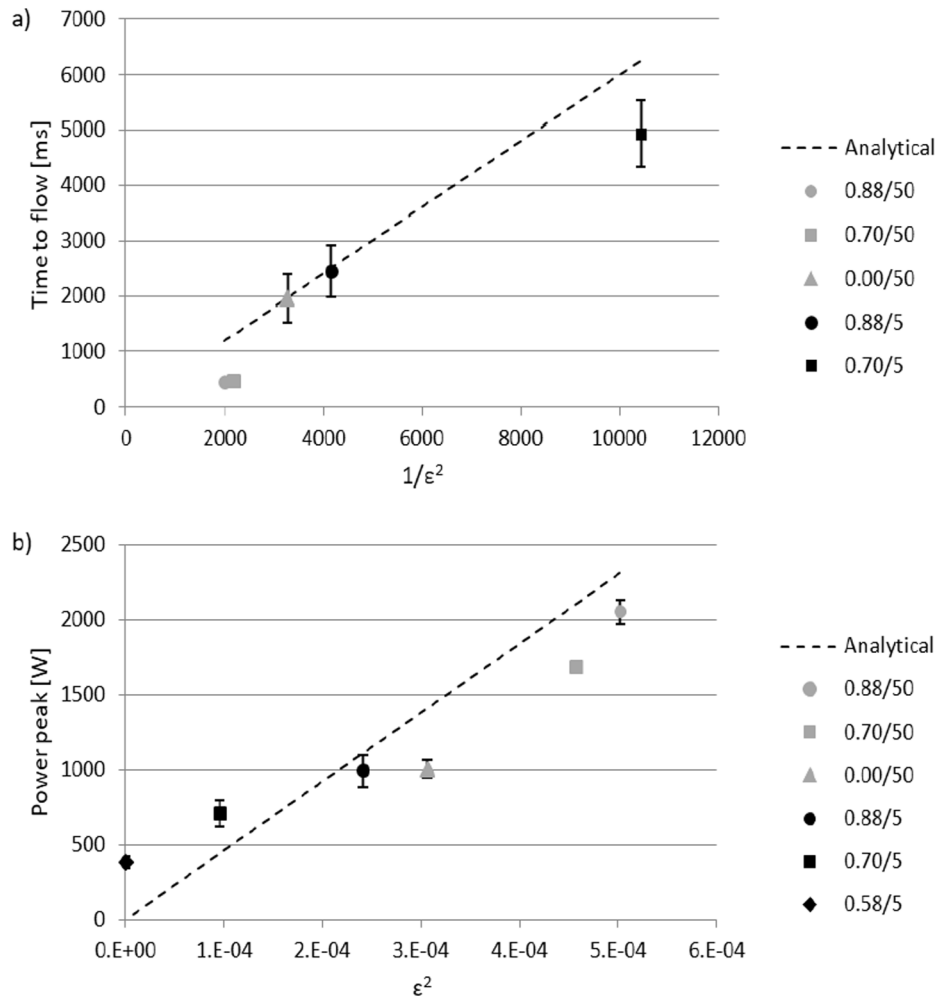


Fig. 14. a) Time to flow versus $1/\epsilon^2$ and b) Power peak versus ϵ^2 . The through-thickness strain obtained from FEM model is used to represent both experimental and analytical data. Analytical time to flow and power peak are calculated using Equations (A.7) and (A.9) in Appendix A. Cases 1.00/5 and 1.00/50 were not simulated in the FEM model and are not included in the plot. Case 0.58/5 is not included in (a) since predicted zero strain results in infinite time to flow.

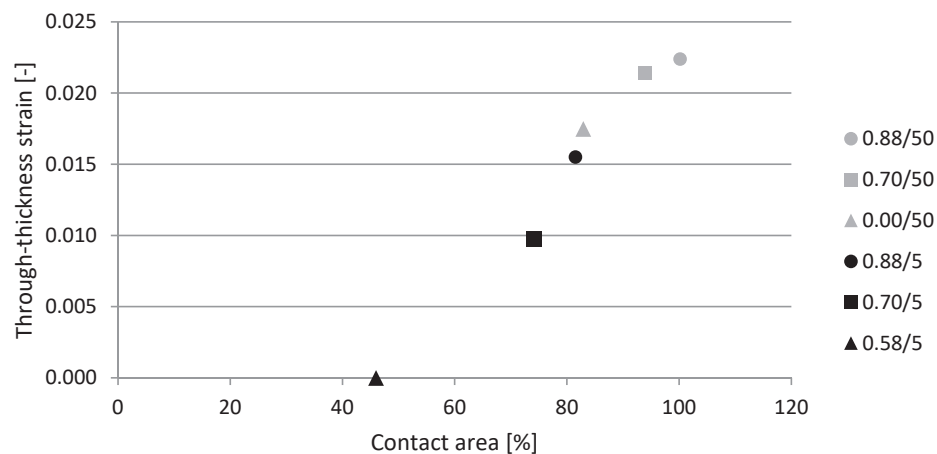


Fig. 15. Through-thickness cyclic strain obtained from the numerical model versus experimentally measured contact area between top adherend and sonotrode.

ultimately, on the through-thickness cyclic strain in the ED. In fact, the deflection of a cantilever beam is proportional to the applied force (i.e., the welding force) and to the cube of the arm length of the beam (i.e., the clamping distance). Under the same welding force, a shorter clamping distance will then result in a smaller deflection of the top adherend and, hence, in a larger angle in the overlap and lower contact between top

adherend and ED. A smaller portion of the amplitude of vibration will be then transmitted to the ED, since part of it will be used to close the pre-existing gap. This effect is however only observed for a normalised supporting base thickness different from 1.00, otherwise no angle between adherends can be created. The decreasing cyclic strain in the ED with decreasing clamping distance, as shown by the difference in

Table 4

Fracture surfaces of the bottom adherend for optimum welds (consolidation applied) obtained with 50 mm clamping distance and different supporting base thicknesses, corresponding angle, optimum displacement (d_{opt}), total duration of vibration phase (heating time) and LSS. Dashed rectangles indicate the overlap area. Position of Edge 1 and Edge 2 for all fracture surfaces is indicated in case 0.88/50.



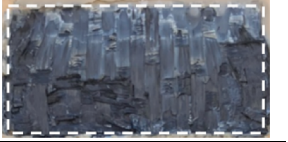
Fracture surfaces			
Case	0.88/50	0.70/50	0.00/50
Angle [°]	0.45 ± 0.18	0.84 ± 0.06	2.57 ± 0.08
d_{opt} [mm]	0.07	0.05	0.03
Heating time [ms]	792.00 ± 71.63	760.67 ± 27.75	2206 ± 259.93
LSS [MPa]	46.98 ± 0.12	44.91 ± 5.09	42.56 ± 1.76

Table A1

Parameters used for the analytical predictions of time to flow and power peak.

Parameters	Symbol	Value	Source
Frequency of vibration	ω	20 kHz	Process input
Friction coefficient	μ	0.17	Estimation based on [28]
Hammering coefficient	α	0.45	Curve fitting*
Efficiency coefficient	χ	0.25	Curve fitting*
ED length	L_{ED}	12.7 mm	Measured
ED area	A_{ED}	322.58 mm ²	Measured
ED volume	V_{ED}	80.65 mm ³	Measured
ED mass	m_{ED}	0.10 g	Measured
Poisson ratio (PEEK)	ν	0.4	[27]
Specific heat (PEEK)	c	1.34 kJ/kg/K	[27]
Elastic modulus (PEEK) at 20 kHz	E'	3.55 GPa	[6]
Elastic modulus (PEEK) at T_g at 20 kHz	E'_{T_g}	3.55 GPa	[6]
Average loss modulus (PEEK) at 20 kHz	E''_{avg}	0.50 GPa	[6]
Loss modulus (PEEK) at T_g at 20 kHz	E''_{T_g}	2.00 GPa	[6]
Room temperature	T_{room}	25 °C	Estimation
Glass transition temperature (PEEK)	T_g	143 °C	[29]
Melting temperature (PEEK)	T_m	343 °C	[29]

* The procedure to obtain these values is described on Section 4.

through-thickness strain between Fig. 8.a and 8.b, is consistent with this hypothesis. Changes in the cyclic strain in the ED will in turn affect ultrasonic heat generation [28] and related variables such as the time to flow or consumed power. These relationships between the cyclic strain and the time to flow and the consumed power were derived as a simplified analytical model presented in Appendix A. Contrary to Fig. 13, Fig. 14 shows unambiguous relationships between the experimental values for the time to flow/power peak and the numerical values for the cyclic strain in the ED. Note that, based on the analytical equations derived in Appendix A, in Fig. 14 the time to flow is plotted against the inverse of the cyclic strain squared and the power peak against the cyclic strain squared.

Also remarkable in Fig. 14 is the relatively close correlation between experimental values and analytical results for the time to flow and power peak, despite the simplifications made in the derivation of the analytical relations in Appendix A. Some of these simplifications are neglecting potential effects of the angle and clamping distance on the hammering coefficient and, hence, on amplitude transmission [22], as well as effects on the actual area contributing to interfacial friction heating. Fig. 14 shows then that, in spite of the complexity of ultrasonic heat generation, relatively simple analytical equations may be used to predict, with certain accuracy, the time to flow and power peak based on the cyclic strain experienced by the ED under a certain set of welding parameters and clamping conditions. The equations in Appendix A are

however limited to the cases where most of the downward displacement of the sonotrode is due to the flow of the ED, since they do not consider the heating and potential flow of the adherends' polymer that might occur for some cases (as it appears to be the case for 0.58/5, which was thus not included in Fig. 14.a). It is important to note that the efficiency of the process and the hammering coefficient were used as fitting parameters. In the work of Levy et al. [28], the authors used an efficiency of 0.13 and a hammering coefficient between 0.32 and 0.39. Considering that a different machine and clamping jig were used in this work, our choice of 0.25 for the efficiency coefficient and 0.45 for the hammering coefficient (see Appendix A) is deemed reasonable. Furthermore, the cyclic strain in the ED can be estimated through either a simplified numerical model (Section 3.2) or by the contact area measurements since Fig. 15 indicates that there exists a linear correlation between the two (both parameters being related to the stiffness of the beam). Additional research is needed to explore this option further.

Regarding the relationship between *weld uniformity* and the angle between the adherends and clamping distance, increasing non-uniformity with increased angle and decreased clamping distance is an effect of the slippage at Edge 2 and contact between the top adherend and the ED at Edge 1 (see Fig. 3). At Edge 2 the ED is compressed by the non-parallel adherends, hence slippage with respect to the surfaces of the adherends is restricted. The numerical results already indicate such hindered slippage for the cases with a short clamping distance, with the localized compressive strain at Edge 2 that occurred even when the sonotrode was at its highest position (Fig. 8.a). Hindered slippage implies hindered heat generation through surface friction, which is mainly responsible for the initial increase in temperature up to the T_g of the material before viscoelastic heating becomes dominant [7,11]. This is consistent with the temperature profiles measured at Edge 2 (Fig. 10) and with the intact ED observed at Edge 2 in Fig. 11.a–c and 12.b. At Edge 1, reduced contact between the ED and the non-parallel top adherend results in part of the vibration being dissipated in the top adherend. This leads to bulk heating and melting of the matrix, which is consistent with the high degree of porosity and resin flow in the top adherend (Fig. 12.b) and with signs of overheating (Fig. 11.b and 11.c) towards Edge 1. Increasing the clamping distance diminishes both effects and results in fully-welded overlaps with uniform weld quality, as seen in Fig. 11.d–f. This occurs due to the lower structural stiffness of the top adherend, which decreases the force that the deformed top adherend applies on Edge 2, allowing slippage between the ED and the adherends surfaces, and improves contact between adherend and ED at Edge 1. Table 4 also shows that the existence of an angle between the adherends still affects some parameters of the process such as optimum sonotrode displacement and heating time even for cases with a larger clamping distance. Decreasing optimum displacement with increasing angle results from the early melting of the matrix in the top adherend, which is consistent with partial dissipation of the vibration in the top adherend owing to the nevertheless presence of an angle. Meanwhile, the increased heating time is a direct result of the decreasing cyclic strain on

the ED that occurs with increased angle (Fig. 14.a). However, decreasing the structural stiffness of the top adherend results in no overheated areas in the fracture surfaces and in an overall uniform aspect, with only the case with the largest angle (0.00/50) among the cases with 50 mm clamping distance presenting some variation between Edge 1 and Edge 2, which was also reflected on lower LSS. At Edge 2, the fracture occurred at the welding interface, as indicated by the lighter tone of the bottom adherend at that area while fracture occurred in the inner layers of the bottom adherend at Edge 1, as one can see by the texture of the fracture in that area. This difference in the fracture surface of the case 0.00/50 compared to cases 0.88/50 and 0.70/50 aligns with the temperature profiles shown in Fig. 10.b. For the smallest angles (0.88/50 and 0.70/50), both edges achieved temperatures above PEEK T_m very early in the process, which is in accordance with the uniform fracture surfaces of these cases. It is interesting to observe that Edge 2 presented even higher temperatures than Edge 1, which can be a result of a positive effect coming from the higher pressure at Edge 2 while not yet hindering the slippage at that area, as explained by Eveno and Gillespie [23]. However, further increasing the angle (0.0/50) resulted in only Edge 1 achieving PEEK T_m , as a consequence of the hindered slippage at Edge 2.

5. Conclusions

In this paper, the influence of misalignment between adherends on static ultrasonic welding of C/PEEK adherends with a flat PEEK energy director was investigated. The different angles between the adherends were created by the clamping configuration, which resulted in angles between 0.20° and 4.50° . The main findings and contributions of this work are the following:

- Increasing the angle affected the ultrasonic welding process by decreasing the average cyclic strain in the ED and by hindering slippage at one of the transverse edges of the overlap. The decreased cyclic strain in the ED caused an increase in the time needed for the onset of the downward movement of the sonotrode and a decrease in the maximum power consumed by the process. The hindered local slippage resulted in a decrease in the weld uniformity.
- A simplified 2D numerical model was developed and can be used to obtain the cyclic strain on the ED. Analytical calculations derived in

this work allow the use of the numerical cyclic strain obtained from the model to predict time to flow and power peak of the different cases studied herein. The use of contact area measurements also showed potential to predict the cyclic strain on the ED for the different cases.

- The angle is not the only parameter affecting the process. The clamping distance also plays an important role since decreasing clamping distance increases the stiffness of the top adherend. The cases with shorter clamping distance presented a longer time to flow, lower power peak and less uniform fracture surfaces than those with a larger clamping distance. Thus, increasing clamping distance mitigates the effects caused by the presence of an angle between the adherends.

CRediT authorship contribution statement

C. B. G. Brito: Conceptualization, Methodology, Formal analysis, Investigation, Visualization, Writing – original draft. **J. Teuwen:** Conceptualization, Writing – review & editing, Supervision. **C.A. Dransfeld:** Resources, Writing – review & editing, Supervision. **I. F. Villegas:** Conceptualization, Data curation, Writing – original draft, Supervision, Funding acquisition.

Declaration of Competing Interest

The authors declare that they have no known competing financial interests or personal relationships that could have appeared to influence the work reported in this paper.

Acknowledgement

The work presented in this paper is carried out as part of a project, which has received funding from the Clean Sky 2 Joint Undertaking (JU) under the European Union's Horizon 2020 research and innovation programme under grant agreement No 776455. The results, opinions, conclusions, etc. presented in this work are those of the author(s) only and do not necessarily represent the position of the JU; the JU is not responsible for any use made of the information contained herein.

Appendix A. Derivation of analytical relationships between through-thickness strain and time to flow and maximum power

Assuming that the energy director (ED) flows when it reaches its melting temperature, the time to flow, t_{flow} , can be expressed as:

$$t_{flow} = \int_{T_{room}}^{T_m} \frac{1}{\dot{Q}} dQ = \int_{T_{room}}^{T_m} \frac{1}{(\dot{Q}_{fric} + \dot{Q}_{visc})} dQ \quad A.1$$

Where Q is the heat generated by the ED, \dot{Q} is the heat generation rate, which consists of an interfacial friction term, \dot{Q}_{fric} , and a viscoelastic friction term, \dot{Q}_{visc} . Assuming that friction heating is mainly responsible for increasing the temperature in the ED from room temperature until the glass transition temperature of the polymer, T_g , [7,11,11,7]; and that, after that, viscoelastic heating becomes the main heat source as adhesion between ED and adherends starts to occur and the contribution of interfacial friction decreases, Equation (A.1) becomes:

$$t_{flow} = \int_{T_{room}}^{T_g} \frac{1}{\dot{Q}_{fric}} dQ + \int_{T_g}^{T_m} \frac{1}{\dot{Q}_{visc}} dQ \quad A.2$$

The viscoelastic heating rate can be estimated according to the following equation [6]:

$$\dot{Q}_{visc} = \chi \alpha \frac{\omega E'' \epsilon_0^2}{2} V_{ED} \quad A.3$$

Where ϵ_0 is the cyclic strain in the ED, α is the hammering coefficient, ω is the vibration frequency, E'' is the loss modulus of the material, V_{ED} is the volume of the ED, and χ is the efficiency of the process, which decreases due to acoustic losses and dissipation in the composite plates and jig [28]. The interfacial heating rate can be estimated according to the following equation [20]:

$$\dot{Q}_{fric} = \chi \alpha \frac{\mu \omega}{\pi} u_0 \sigma_0 A_{ED} \quad A.4$$

Where μ is the friction coefficient, σ_0 is the normal stress, u_0 is the relative movement (slippage) between surfaces and A_{ED} is the surface area of the ED. The normal stress and the slippage are given by the following equations:

$$u_0 = \frac{\varepsilon_0}{\nu} L_{ED} \quad \text{A.5}$$

$$\sigma_0 = E' \varepsilon_0 \quad \text{A.6}$$

in which ν is the Poisson's ratio of the ED, L_{ED} is the length of the ED within the overlap and E' is the elastic modulus of the ED.

Assuming that \dot{Q}_{fric} and \dot{Q}_{visc} are temperature independent and introducing Equations (A.3) and (A.4) in Equation (A.2), the time to flow results:

$$t_{flow} = \left(\frac{(T_g - T_{room})}{\frac{\mu}{\pi} A_{ED}} \frac{1}{\left(\frac{L_{ED}}{\nu}\right) E'} + \frac{(T_m - T_g)}{\frac{E'_{avg}}{2} V_{ED}} \right) \frac{m_{ED} C_{ED}}{\chi \alpha \omega \varepsilon_0^2} \quad \text{A.7}$$

Where m_{ED} and C_{ED} are the mass and the specific heat of the ED, respectively ($Q = m_{ED} C_{ED} \Delta T$) and E'_{avg} is the average loss modulus between T_g and T_m (following procedure in [6] to account for temperature dependence of the loss modulus).

The power occurring at any moment during the process [28] is given by:

$$P = \left(\dot{Q}_{fric} + \dot{Q}_{visc} \right) = \chi \alpha \omega \varepsilon_0^2 \left(\frac{\mu E'}{\pi \nu} + \frac{E''}{2} \right) V_{ED} \quad \text{A.8}$$

The power peak, P_{peak} , i.e., maximum power occurring during the process, is assumed to correspond to the moment in the process in which the loss modulus reaches its maximum value, E'_{T_g} , i.e., around the T_g of the polymer material. Hence, the power peak is given by the following equation:

$$P_{peak} = \left(\dot{Q}_{fric} + \dot{Q}_{visc} \right) = \chi \alpha \omega \varepsilon_0^2 \left(\frac{\mu E'_{T_g}}{\pi \nu} + \frac{E'_{T_g}}{2} \right) V_{ED} \quad \text{A.9}$$

All values used for the analytical predictions based on Equations (A.7) and (A.9) are shown in Table A1.

References

- [1] Díaz J, Rubio L. Developments to manufacture structural aeronautical parts in carbon fibre reinforced thermoplastic materials. *J. Mater. Process. Technol.* 2003; 143-144:342-6.
- [2] Chang IY, Lees JK. Recent development in thermoplastic composites: A review of matrix systems and processing methods. *J. Thermoplast. Compos. Mater.* 1988;1 (3):277-96.
- [3] Yousefpour A, Hojjati M, Immarigeon J-P. Fusion bonding/welding of thermoplastic composites. *J. Thermoplast. Compos. Mater.* 2004;17(4):303-41.
- [4] Roux M, Eguémann N, Dransfeld C, Thiébaud F, Perreux D. Thermoplastic carbon fibre-reinforced polymer recycling with electrodynamic fragmentation: From cradle to cradle. *J. Thermoplast. Compos. Mater.* 2017;30(3):381-403.
- [5] C. Georges, L. Ye and M. Hou, "Advances in fusion techniques for joining thermoplastic matrix composites: a review," *Composites: Part A*, pp. 839-857, 2001.
- [6] Benatar A, Gutowski T. Ultrasonic welding of PEEK graphite APC-2 composites. *Polym. Eng. Sci.* 1989;29(23):1705-21.
- [7] Zhang Z, Wang X, Luo Y, Zhang Z, Wang L. Study on heating process of ultrasonic welding for thermoplastics. *J. Thermoplast. Compos. Mater.* September 2010;23: 647-64.
- [8] Tolunay MN, Dawson PR, Wang KK. Heating and Bonding Mechanisms in Ultrasonic Welding of Thermoplastics. *Polym. Eng. Sci.* 1983;23(13):726-33.
- [9] C. Nonhof and G. Luiten, "Estimates for process conditions during the ultrasonic welding of thermoplastics," *Polymer Engineering and Science*, vol. 36, pp. 1177-1183, Mid-May 1996.
- [10] Li Y, Liu Z, Shen J, Lee T, Banu M, Hu S. Weld quality prediction in ultrasonic welding of carbon fiber composite based on an ultrasonic wave transmission model. *J. Manuf. Sci. Eng.* 2019;141.
- [11] Villegas IF. In situ monitoring of ultrasonic welding of thermoplastic composites through power and displacement data. *J. Thermoplast. Compos. Mater.* 2015;28 (1):66-85.
- [12] Villegas IF. Strength development versus process data in ultrasonic welding of thermoplastic composites with flat energy directors and its application to the definition of optimum processing parameters. *Compos. A* 2014;65:27-37.
- [13] Jongbloed B, Teuwen J, Palardy G, Fernandez Villegas I, Benedictus R. Continuous ultrasonic welding of thermoplastic composites: Enhancing the weld uniformity by changing the energy director. *J. Compos. Mater.* 2020;54(15):2023-35.
- [14] Palardy G, Villegas I. On the effect of flat energy director thickness on heat generation during ultrasonic welding of thermoplastic composites. *Compos. Interfaces* 2017;24:203-14.
- [15] Villegas I, Valle Grande B, Bersee H, Benedictus R. "A comparative evaluation between flat and traditional energy directors for ultrasonic welding of CF/PPS thermoplastic composites", *Compos. Interfaces* 2015;8:1-13.
- [16] Zhao T, Broek C, Palardy G, Villegas IF, Benedictus R. Towards robust sequential ultrasonic spot welding of thermoplastic composites: Welding process control strategy for consistent weld quality. *Compos. Part A* 2018;109:355-67.
- [17] Jongbloed B, Teuwen J, Benedictus R, Villegas IF. On differences and similarities between static and continuous ultrasonic welding of thermoplastic composites. *Compos. B* 2020;203:108466. <https://doi.org/10.1016/j.compositesb.2020.108466>.
- [18] Veldman S, Kortbeek P, Wölcken P, Herrmann R, Kos J, Villegas I. Development of a multifunctional fuselage demonstrator. *Aerospace Europe Conference* 2020.
- [19] Senders F, van Beurden M, Palardy G, Villegas IF. Zero-flow: a novel approach to continuous ultrasonic welding of CF/PPS thermoplastic composite plates. *Adv. Manuf. Polym. Compos. Sci.* 2016;2(3-4):83-92.
- [20] Tutunjian S, Dannemann M, Fischer F, Eroglu O, Modler N. A Control Method for the Ultrasonic Spot Welding of Fiber-Reinforced Thermoplastic Laminates through the Weld-Power Time Derivative. *JMMP* 2018;3:1. <https://doi.org/10.3390/jmmp3010001>.
- [21] Villegas IF, van Moorleghe R. Ultrasonic welding of carbon/epoxy and carbon/PEEK composites through a PEI thermoplastic coupling layer. *Compos. A* 2018; 109:75-83.
- [22] Palardy G, Shi H, Levy A, Le Corre S, Fernandez Villegas I. A study on amplitude transmission in ultrasonic welding of thermoplastic composites. *Compos. Part A* 2018;113:339-49.
- [23] Eveno E, Gillespie J. Experimental investigation of ultrasonic welding of graphite reinforced polyetheretherketone composites. *Proceedings of the National SAMPE Technical Conference*. 1989.
- [24] Benatar A, Eswaran R, Nayar S. Ultrasonic Welding of Thermoplastics in Near-Field. *Polym. Eng. Sci.* 1989;29(23):1689-98.
- [25] Gardiner G. Proving out LM PAEK welding for Multifunctional Fuselage Demonstrator. *Composites World* 2020;27:02.
- [26] Mason H. Moving forward on the Multifunctional Fuselage Demonstrator (MFFD). *Composites World* 2020;28:10.
- [27] Goodfellow, "Polyetheretherketone PEEK Material Information," [Online]. Available: <http://www.goodfellow.com/E/Polyetheretherketone.html>. [Accessed 2020].
- [28] Levy A, Le Corre S, Villegas I. Modeling of the heating phenomena in ultrasonic welding of thermoplastic composites with flat energy directors. *J. Mater. Process. Technol.* 2014;214:1361-71.
- [29] Pilato LA, Michno MJ, editors. *Advanced Composite Materials*. Berlin, Heidelberg: Springer Berlin Heidelberg; 1994.